THE ASTROPHYSICAL JOURNAL, 429:736–747, 1994 July 10

A NEW MEASUREMENT OF THE FLUX OF THE LIGHT COSMIC-RAY NUCLEI AT HIGH ENERGIES

J. BUCKLEY,[1] J. DWYER,[1] D. MÜLLER, AND S. SWORDY
Enrico Fermi Institute and Department of Physics, University of Chicago, 5640 South Ellis Avenue, Chicago, IL 60637
AND
K. K. TANG
Department of Physics, University of Utah, Salt Lake City, UT 84112
Received 1993 October 25; accepted 1994 January 10

ABSTRACT

A new cosmic-ray detector utilizing a ring-imaging Čerenkov counter to determine the energy of light cosmic-ray nuclei was flown on a high-altitude balloon from Fort Sumner, NM, in 1991 September. We describe the design and performance of this instrument and discuss the data analysis procedures. The measurement provides a new determination of the absolute flux and differential energy spectrum of the primary cosmic-ray species helium between 40 and 320 GeV nucleon^{-1}. The experiment also yields the spectra of carbon and oxygen and some information on the intensities of the secondary nuclei Li, Be, and B. A comparison between our results and previous measurements of heavier nuclei ($Z \geq 4$) from *HEAO 3* and Spacelab 2 indicates good consistency between these measurements. The data set is compared with the results of a leaky box propagation model. We find good agreement with this model if the abundance of helium relative to oxygen at the source is taken to be 25 ± 6 and if the source spectrum is given by a power law in energy proportional to $E^{-2.15}$.

Subject heading: cosmic rays

1. INTRODUCTION

It is now generally believed that diffusive shock acceleration in supernova remnants can account for the observed flux of galactic cosmic rays to energies of at least 10^{14} eV. The power budget is satisfied if the efficiency for converting the energy of the supernova explosion is of the order of a few percent. In this model, particles are accelerated by the first-order Fermi process resulting in power-law spectra in rigidity R proportional to $R^{-\alpha}$. The spectral slope α depends only on the strength of the shock and is in rough agreement with that inferred from observations. Still poorly understood, however, are the injection mechanism and the details of the elemental composition at the source. The value of the maximum energy is also the subject of debate due primarily to uncertainties in the magnetic field structure around the shock. Extensions of the simple model might well result in deviations from a power-law spectrum or in changes in the composition with energy (Ellison 1993). Key to resolving these issues are precision measurements with high statistics of the elemental composition and spectral shape of cosmic-ray nuclei.

To derive the cosmic-ray spectra at the source, the measured data near Earth must be corrected for the propagation of the cosmic rays through the Galaxy. These corrections include the effect of nuclear interactions in the interstellar medium, the rigidity dependent escape from the Galaxy, energy loss processes during propagation as well as possible secondary acceleration, and the local effects of solar modulation. At energies below ~ 10 GeV nucleon^{-1} these corrections are less certain than at higher energies since the cross sections for spallation of cosmic rays in the interstellar medium are dependent on energy and are often not well measured, and, in addition, ionization energy loss can significantly alter the shape of the spectrum. Solar modulation also has a strong effect in this energy region.

Therefore, to derive the energy spectra and composition *at the source* measurements at high energy are highly desirable. In recent years fairly consistent measurements of the energy spectra of cosmic-ray hydrogen (Ryan, Ormes, & Balasubrahmanyan 1972; Asakimori et al. 1993) and those of the nuclei heavier than boron (Engelmann et al. 1990; Müller et al. 1991) have been reported. An exception is helium, where the uncertainties are still rather large despite helium being the second most abundant element.

The major challenge in any measurement of high-energy cosmic rays is to find an experimental technique which has both a calibrated response with energy and well-known fluctuations in the measured quantities. The latter requirement is extremely important since improper accounting for the fluctuations can lead to significant errors in determining the spectrum from the observed signals.

Detectors such as magnetic spectrometers and total absorption calorimeters are impractical for such measurements because of their large weight. Calorimeters with a small number of interaction lengths of material give rise to large fluctuations in the measured energy. Detectors which have the advantage of low mass and are well calibrated are integrating Čerenkov counters and transition radiation detectors (L'Heureux et al. 1990). These, however, are of limited value for low-Z particles such as helium since the signals produced are then quite small and the signal fluctuations limit the accuracy of the measurements. To alleviate some of these problems, we have applied the technique of ring imaging Čerenkov counters (RICH) for a measurement of the energy spectra and flux levels of light cosmic-ray nuclei. This technique relies on the mea-

[1] In partial fulfillment of the requirements for the Ph.D. degree at the Department of Physics, University of Chicago.

surement of the Čerenkov angle for each particle which can be determined with high accuracy even if only a few Čerenkov photons are detected.

Our detector was flown for the first time on a high-altitude balloon in 1991. This paper describes the instrument, discusses the data analysis procedures, and presents the results from this flight. A brief description of the technique was already given by Buckley et al. (1992), and preliminary results were presented by Buckley et al. (1993) and Dwyer et al. (1993).

2. EXPERIMENTAL PRINCIPLES—THE RING IMAGING TECHNIQUE

When a charged particle traverses a medium at a velocity greater than the velocity of light in the medium, Čerenkov light is emitted at a characteristic angle with respect to the particle trajectory, and from a measurement of the Čerenkov angle one may determine the Lorentz factor of the particle. For gas counters, with Čerenkov thresholds typically corresponding to energies of 10 to 100 GeV nucleon^{-1}, the maximum Čerenkov angles are small, of the order of a few degrees.

In our instrument, Čerenkov light emitted along the particle path is imaged by a spherical mirror into a ring on a position sensitive photon detector in the focal plane (see Fig. 1). From the radius r of the ring image we determine the Čerenkov angle θ_c and with it the Lorentz factor γ:

$$\sin^2 \theta_c \approx \theta_c^2 \simeq \frac{1}{\gamma_0^2} - \frac{1}{\gamma^2}, \qquad (2.1)$$

where the Lorentz factor threshold, γ_0, is related to the index of refraction of the radiator as $\gamma_0 = n/(n^2 - 1)^{1/2}$. We use nitrogen as a radiator, where $\gamma_0 \approx 40$ at 1 atmosphere (see § 4.3.1).

A precise measurement of the particle trajectory is necessary to predict the ring center in the focal plane of the RICH counter. This is essential (*a*) for the determination of the ring radius for events with a small number of detected photons and (*b*) for a strong suppression of background signals since only photon detector signals in a region around the ring center need to be accepted for analysis. Together with a measurement of the particle trajectory, a RICH counter provides a measurement of the Čerenkov angle *for each detected photon.* Unlike integrating Čerenkov counters that depend on a measurement of the total light intensity, this means that the Lorentz factor of the incident cosmic ray can be determined with precision even if just one photon is detected. Another important feature of this detector is the fact that charge and energy measurements are decoupled: the Čerenkov angle depends only on γ while the total number of photons scales with Z^2. This is in contrast to integrating counters which measure only the light intensity such that a mistaken charge assignment also results in an error in the energy determination.

It is interesting to note that the RICH technique is exceptionally well calibrated: the energy measurement requires only knowledge of the geometry of the instrument and of the index of refraction of the radiator. For cosmic rays with a continuous energy spectrum, even the value of the index of refraction can be confirmed with the data by determining the maximum Čerenkov angle, i.e., $\theta_{max} = 1/\gamma_0^2$ for $\gamma \to \infty$.

3. INSTRUMENTATION AND THE BALLOON FLIGHT

A schematic cross section of the instrument is shown in Figure 2. We briefly summarize its principal features in the following. The main detector components are: (1) two scintillation counters, located at the top and bottom of the instrument, to provide a coincidence trigger and a measurement of the nuclear charge, (2) a hodoscope consisting of eight drift chambers (four chambers above and below the Čerenkov counter, respectively) to determine the particle trajectory and to provide an additional charge measurement, and (3) a ring imaging Čerenkov counter to measure the Lorentz factor of the particle. This counter consists of a combination of a spher-

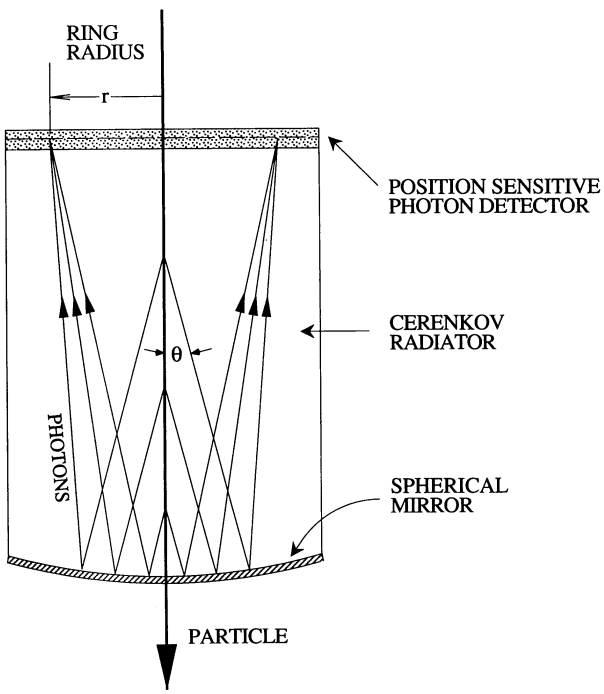

FIG. 1.—Principle of the ring imaging Čerenkov technique

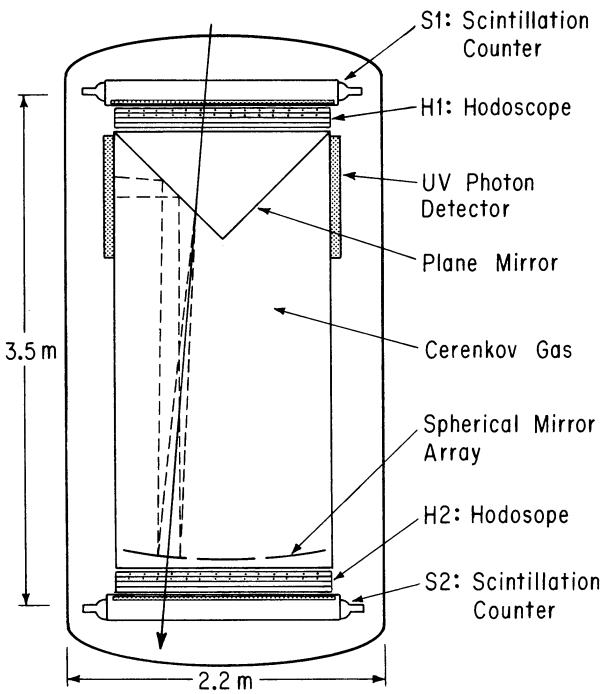

FIG. 2.—Schematic cross section of the instrument

ical mirror and a plane mirror assembly, which focuses the Čerenkov light produced in the gas radiator onto position-sensitive UV photon detectors.

The scintillation counters (S1, S2) provide the primary measurement of the nuclear charge, utilizing the Z^2 dependence of the ionization loss in the scintillators. Each counter consists of 1.5×1.5 m^2 of acrylic scintillator (1 cm thick) enclosed in a 15 cm high light-integration box. The insides of these boxes are painted with high reflectivity white paint (Kodak 6080) to improve the light collection efficiency across the detector. The scintillation light in each detector is viewed by 12 RCA 4525 photomultiplier tubes (PMT) with 13 cm diameter photocathodes. The signals from the PMT anodes are amplified and summed for each scintillation counter. Coincidences between these signals from the top and bottom scintillators trigger the instrument and provide a timing reference for the drift chambers that are employed in the hodoscope and photon detector. The signals from the last dynode of the PMTs are individually digitized by 8 bit pulse height analyzers to provide 12 independent measurements of the light yield in each counter.

The hodoscope assemblies (H1, H2) consist of eight layers of Ar/CH_4-filled drift chambers with thin aluminized Mylar windows. Each chamber has an area of 150 cm $\times$ 150 cm and is divided into seven horizontal drift cells, each with a 25 μm sense wire. The aluminized Mylar windows are etched into strips which are connected to a voltage divider producing a uniform drift field in each cell (see Fig. 3). The signal on each wire is digitized with 2 bit resolution in 33 ns time intervals up to a total of 248 time slices after the instrument trigger. In addition, the overall charge signals induced on the cathode strips adjacent to the sense wires are pulse height analyzed with 12 bit resolution to provide a total of eight measurements of the ionization loss for each event. For each chamber, the drift time and wire number determine the position of the primary ionization track in the direction perpendicular to the sense wires with an accuracy of about 1 mm.

For each layer of the hodoscope, there is an adjacent layer with parallel sense wires, offset by half of a cell width (see Fig. 3). This arrangement allows the left-right ambiguity in the direction of drift to be resolved, in addition to providing redundancy in the position and charge measurement. There are two assemblies of four chambers at each end of the instrument, each providing two measurements of the x-coordinate and two measurements of the y-coordinate.

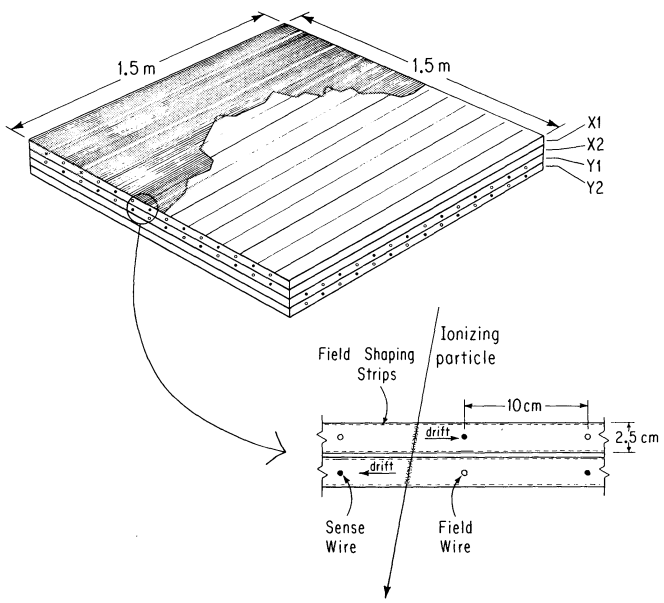

FIG. 3.—Schematic view of one of the two hodoscope assemblies

The Lorentz factor of the cosmic ray is determined by the central RICH counter. For each particle above the Čerenkov threshold, Čerenkov photons are emitted in the gas radiator which is filled with pure nitrogen at atmospheric pressure. The photons are focused by an array of UV-reflective spherical mirrors into a ring on the focal plane detectors. These detectors are placed out of the path of the cosmic ray, by rotating the focal plane to the sides of the instrument using plane mirrors inclined at 45°. In the focal plane, position-sensitive UV photon detectors record the individual Čerenkov photons in the ring.

The photon detectors, shown schematically in Figure 4, are based largely on a design used at the CERN OMEGA spectrometer (Apsimon et al. 1985a, b). They consist of two 1.5 m $\times$ 0.75 m drift chambers filled with ethane gas and made photosensitive by a small admixture of TMAE [tetrakis (dimethylamino) ethylene] (Anderson 1981, 1982). TMAE has a photoionization potential of 5.36 eV, corresponding to a wavelength threshold of 2310 Å (see, e.g., Holroyd et al. 1987). The chambers are 5 cm deep which at a TMAE partial pressure of 1 torr corresponds to about one absorption length for UV photons. Each Čerenkov photon entering the chambers through fused silica windows may produce a single photoelectron. A uniform electric drift field is generated by a set of thin wires, stretched parallel on both sides of the entrance window, and by parallel strips of copper on a printed circuit board which forms the back plane of the chamber. The wires and the copper strips are connected to a resistive voltage divider chain, with a maximum voltage of 8 kV. The photoelectron then drifts toward an array of sense wires. The photon detectors use a total of 1536 sense wires, at a spacing of 4 mm. The wire number and drift time determine the coordinates of the photon conversion point with a resolution of 1.2 mm (rms).

Among the technological challenges of this arrangement are the high proportional amplification gains required at the sense wires to permit efficient detection of single photoelectrons, and an optical "shielding" of the sense wires to reduce feedback from photons produced in the avalanche near the wire. Another challenge is the design of a safe and reliable gas purging system for the TMAE mixture.

While TMAE vapor exhibits high quantum efficiency ($\sim$40% at 1900 Å), it is highly corrosive and reacts strongly with oxygen. For our detector, a system is used in which ethane gas is bubbled through clean liquid TMAE at a temperature of 12 ± 0.1° C. The photon detectors are continuously purged with this gas mixture, and the outflow from the chamber is passed through a cold trap filled with dry ice and ethanol to freeze out the TMAE vapor before the gas emerges into the balloon gondola. This system prevents the condensation of TMAE on the chamber walls or windows as long as the chamber structures have a higher temperature than the bubbler.

A block diagram of the flight electronics is shown in Figure 5. The acquisition of data is initiated by the trigger from the scintillator coincidence. Signals from the photon detectors and hodoscope sense wires are analyzed in time slices up to the maximum drift time to allow detection of multiple hits on any

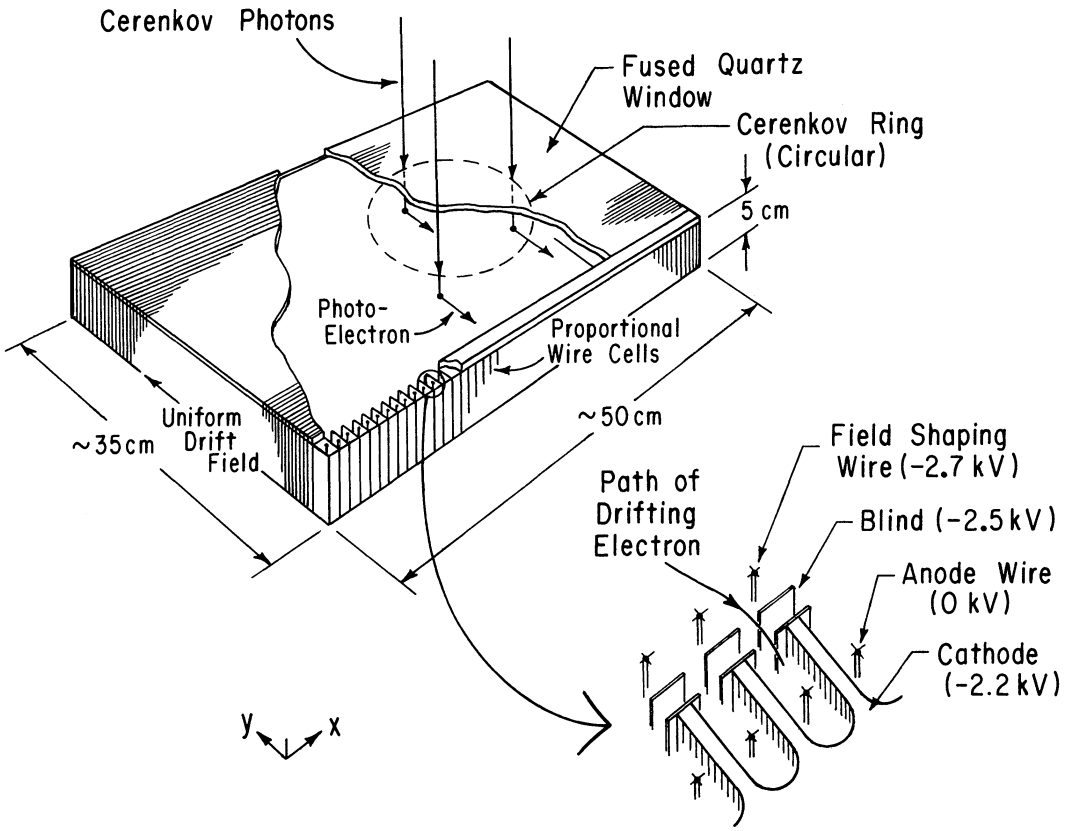

FIG. 4.—Schematic view of a photon chamber module (a total of 12 modules are employed in the detector). The inset shows the electrostatic blind structure to prevent photon feedback.

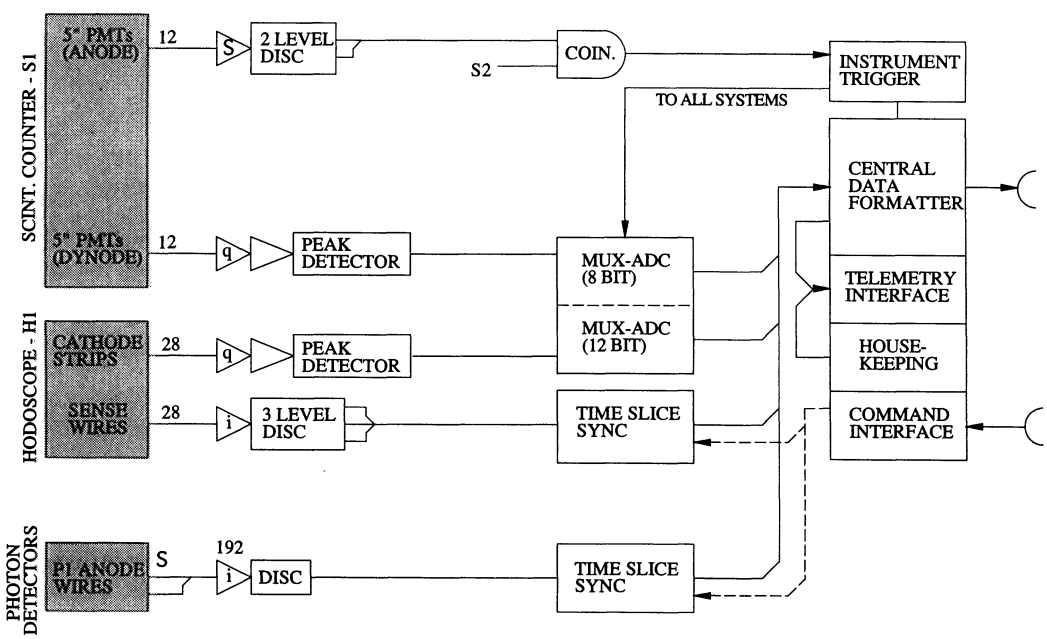

FIG. 5.—Block diagram of the flight electronics

wire. The sense wires are fed into amplifier/discriminator pairs, digitized with a time resolution of 83 ns and 33 ns for the photon detector and the hodoscope, respectively, and then stored in fast, CMOS first-in-first-out (FIFO) memory devices. To keep dead time to a minimum, the data are immediately transferred to a second set of FIFOs where the data are compressed by zero suppression and by encoding the time and position of the hits.

Simultaneously, the signals from the photomultiplier dynodes and the hodoscope cathodes are pulse height analyzed by another electronic subsystem. Each of these signals is first integrated by charge-sensitive shaping amplifiers and then digitized.

The main electronics polls the subsystems and organizes the data into the final event format in a further set of FIFO memory devices. Further processing organizes the data, event by event, into a storage buffer which is used to feed the data to the telemetry system. This consists of a serial link at 455 kbit s^{-1} to the ground station where the data are recorded on tape for further analysis.

In its first balloon flight in 1991 September from Fort Sumner, New Mexico, the instrument floated for approximately 30 hr at an altitude with an average of 6.2 g cm^{-2} of residual atmosphere, and was recovered near El Paso, Texas.

4. DATA ANALYSIS

4.1. *Trajectory Reconstruction*

Essential to the data analysis is a precise determination of the particle trajectory through the instrument. An ideal cosmic-ray event produces a single ionization signal on each of the eight layers of the hodoscope. If the drift properties of the hodoscope chambers are well understood, the trajectory can be uniquely reconstructed. However, for real events, spurious signals from electronic noise or from knock-on electrons, or multiple tracks after nuclear interactions complicate the reconstruction. To minimize trajectory confusion due to such background, three aspects of the hodoscope design are essential: (1) multiple hit sensitivity of the electronics, (2) redundant measurements by adjacent hodoscope chambers, and (3) measurement of the ionization level corresponding to each hit.

These features permit a comparison of the time and amplitude structure of the signals measured in adjacent hodoscope layers. An algorithm is developed that determines quantitatively the goodness of the correlation and thereby selects the most probable position of the cosmic-ray track. The accuracy in the track determination is further improved with the aid of detailed drift velocity maps that were derived from the flight data. The resulting spatial resolution (rms) was found to be 1.1 mm for helium nuclei, and 0.9 mm for oxygen. In the subsequent analysis, we confirmed this resolution by comparing the measured position of Čerenkov rings with the position of the ring center predicted by the hodoscopes. It is to be noted that even though for high Z nuclei the δ-ray production is greatly increased, we do not observe any degradation of the spatial resolution with increasing nuclear charge.

4.2. *Charge Determination*

The nuclear charge of each cosmic-ray particle is identified from the ionization loss measurements in two plastic scintillators, and in eight gas-filled drift chambers which comprise the hodoscope. Spatial maps of the scintillator response are produced for each individual PMT using the helium data from the flight. The signals from the PMTs for each scintillation counter are combined after corrections are made using these

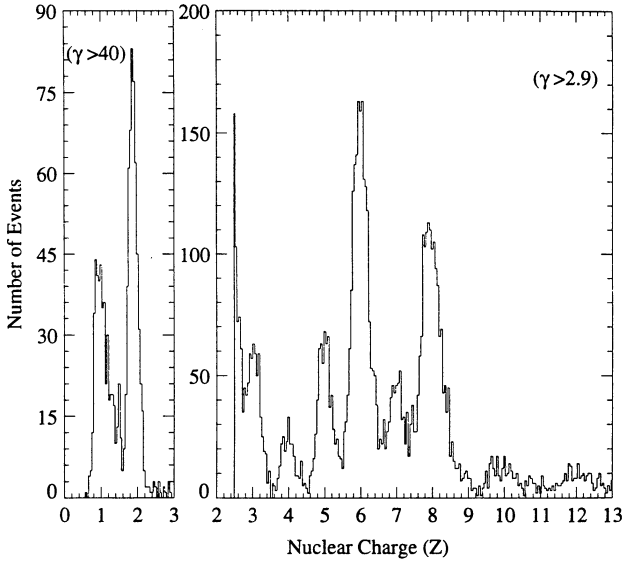

FIG. 6.—Charge distribution observed in flight. Data for $Z \leq 2$ are from events above the Čerenkov threshold. For heavier nuclei ($Z \geq 3$) events above the local geomagnetic cutoff are shown. Protons are suppressed because the trigger threshold was chosen to predominantly select $Z \geq 2$ for this flight.

response maps. Similarly, response maps of the hodoscope drift cells are produced using the flight data and are used to correct the pulse height measurements made by the eight drift chamber layers. Using the angle of incidence measured by the hodoscope, the scintillator and hodoscope signals are normalized to yield the ionization per unit path length.

The charge is found by comparing the corrected pulse height information with measured response functions $P_i(x_i, Z)$ which give the probability of a cosmic ray with charge Z to produce a pulse height x_i. For both the scintillation counters and the hodoscopes, these probability distributions are asymmetric toward large pulse heights. The pulse height measurements are therefore analyzed with a maximum likelihood technique in which we approximate the probability distribution by

$$P(x_i, Z) = \frac{1}{\sqrt{2\pi}} \exp\left[-\frac{1}{2}(\lambda + e^{-\lambda})\right], \tag{4.1}$$

where

$$\lambda \equiv \frac{x_i - Z^2\mu}{Z^2\xi},$$

and ξ and μ are the free-fit parameters.[2] The most likely value of Z^2 is then found by determining the maximum of the likelihood function

$$L = \prod_{i=1}^{N} P(x_i, Z), \tag{4.2}$$

for each event, treating Z as a noninteger variable.

The charge spectrum obtained in this fashion is shown in Figure 6. In order to discriminate against nuclear interactions in the instrument, we require consistency in the charge measurements between the hodoscopes and between the top and bottom scintillators. For helium and oxygen nuclei the allowed deviations of the scintillation signals from the expected means for these charges are $\sim$40% and $\approx$15%, respectively. These

[2] In the limit of a large number of ionizing interactions, this distribution becomes the Landau distribution with ξ and μ determined by the properties of the detector.

cuts retain 85% of the helium events and 90% of the oxygen events while effectively rejecting interactions.

4.3. *Energy Measurements*

4.3.1. *Determination of the Čerenkov Threshold*

In contrast to most other types of particle detectors, ring imaging Čerenkov counters do not require the use of particle accelerators to calibrate their energy response. In order to accurately determine the Čerenkov angle and hence the particle's Lorentz factor the only quantities necessary to know are the dimensions of the instrument and the index of refraction, $n = 1 + \eta$ of the radiator gas.

The range of wavelengths over which this detector is sensitive (1700 to 2200 Å) is limited by absorption in the fused silica window at short wavelengths, and by the photoionization threshold of TMAE at longer wavelengths. Data on dispersion in this region (Wilkinson 1960) show that uncertainties in the energy resolution of the instrument due to dispersion are insignificant compared with other systematic limitations in our measurement and least at most to 0.5 mm fluctuations about the mean ring radius.

The index of refraction also depends on the temperature, T, and pressure, P as

$$\eta \propto \frac{p}{T} . \tag{4.3}$$

The temperature varied by 6° C over the length of the flight and the pressure in the radiator, controlled by an active system during the flight, fluctuated by ± 5 torr about a mean value of 670 torr. Temperature and pressure sensors determined p and T for each event, and corrections for the fluctuations were applied to the data.

The Lorentz factor threshold γ_0 is calculated from the index of refraction, as a weighted average over the wavelength range of the instrument. This takes variations of detector quantum efficiency and optical component properties with wavelength into account. For nitrogen gas, at the average temperature and pressure during the flight, we find $\gamma_0 = 41.7$, corresponding to a maximum possible ring radius of 7.2 cm.

4.3.2. *Measurement of the Ring Radius*

The ring center can be predicted from the cosmic-ray trajectory, by tracing the trajectory through the instrument to the point given by the average photon absorption depth in the photon detector volume.

For each event, the area in the photon detector surrounding the predicted center, within a radius of 15 cm, is searched for the presence of photon "hits." For events with one, two, or three hits, the radial distance of every hit from the ring center is found and the ring radius for that event is then given by the mean of these radii. For events with four or more hits, a circle is fitted to the data and the most likely radius is found. This is done by minimizing the function

$$\chi^2 \equiv \frac{x_c^2}{\sigma_{x_c}^2} + \frac{y_c^2}{\sigma_{y_c}^2} + \sum_{i=1}^{N} \frac{[r - \sqrt{(x_i - x_c)^2 + (y_i - y_c)^2}]^2}{\sigma_r^2} . \tag{4.4}$$

Here σ_{x_c} and σ_{y_c} are the errors in determining the x and y coordinates of the ring center from the measurement of the particle trajectory, (σ_{x_c}, $\sigma_{y_c} \approx 2.6$ mm), σ_r is the error in detecting the position of one photon, (x_i, y_i) are the coordinates of the detected photon "hits," and the fit parameters x_c, y_c and r are, respectively, the ring center coordinates and the ring radius.

We determine σ_r from the flight data using events with a large number of photon hits to which a circle can be easily fitted. From the distribution of the residual radial deviations of individual photon position from the fit circle (see Fig. 7), we obtain σ_r to be 3.0 mm. Thus the total error in measuring the ring radius for one detected photon is about 4 mm. In Figure 8, we show typical Čerenkov rings as obtained for several individual cosmic-ray events.

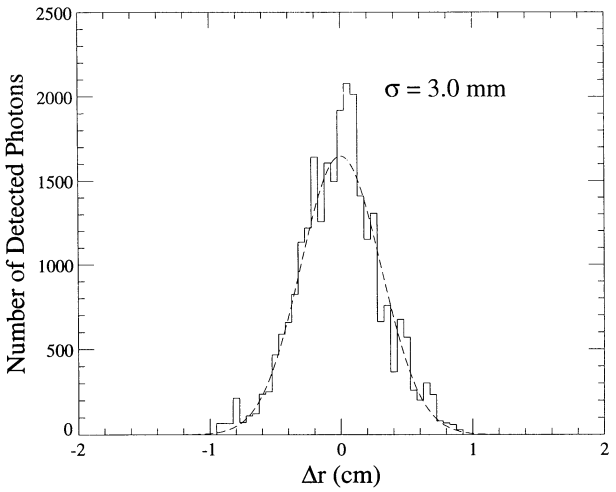

FIG. 7.—Distribution of the radial deviations of detected photons from the best-fit ring radii.

Extremely off axis particles will produce slightly distorted rings. The major effect is to elongate the ring shape in one direction creating an ellipse instead of a circle. This results in a larger average ring radius for an off-axis particle than for particles with vertical trajectories. For example, an extremely off axis particle traversing the instrument will have a ring roughly

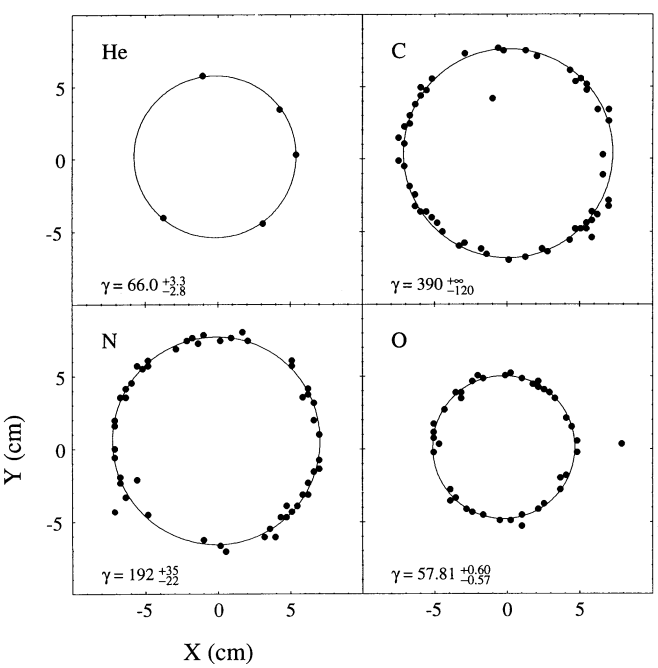

FIG. 8.—Photon detector ring images for individual He, C, N, and O events. The origin of the coordinate system is the ring center position predicted by the hodoscope trajectory measurement. Each point corresponds to a single detected photoelectron. The circles indicated are ring fits obtained from the data analysis procedure, which also determines the Lorentz factors including error limits as shown.

3% larger than a similar particle with a vertical trajectory through the center of the instrument. For helium, the number of detected photons is too small to make the fit of an ellipse to the data practical. Instead, from the knowledge of the trajectory a small correction is made to the measured ring radius, based upon a Monte Carlo simulation of the effect of off-axis particles.

4.3.3. *Background*

It is essential to assess the magnitude of background contributions that could affect the data. Of particular concern is background that consists of spurious signals in the Čerenkov counter that either might simulate the presence of a Čerenkov ring for a low-energy particle (below the Čerenkov threshold) or may appear together with a true Čerenkov ring of a high-energy particle. In either case, such background would lead to a false energy assignment. Because of the steeply falling energy spectrum, our measurement can be successful only if it is highly immune to such background.

As compared to traditional, integrating Čerenkov counters which are sensitive to all *isotropic* background light (produced, for example, as scintillation or Čerenkov light by charged particles passing through the walls of the radiator volume) the RICH device will accept only the fraction of this light which happens to reach the region of an expected Čerenkov ring. For our counter geometry, this fraction is about 0.4%, and this background contribution is therefore negligible.

However, a source of background which must be dealt with are ionizing particles passing directly through the photon detectors such as cosmic-ray particles in chance coincidence with the instrument trigger or energetic δ-rays produced by the incident particle. For instance, for helium we find about eight such background events for every true event above the Čerenkov threshold.

Fortunately, such events leave signatures in the photon detectors which are very different from Čerenkov light. This is illustrated in Figure 9. We therefore reduce this background by cuts, discussed below, on the photon detector image. The efficiency and background rejection power of these cuts have all been verified by Monte Carlo simulations. These simulations incorporate details of the detector responses and the precise geometry of the RICH payload to simulate real events. The validity of this simulation is tested by direct comparison of calculated distributions, such as the deviation of individual photoelectron positions from the fitted ring, with the flight data. Background in the photon detectors is simulated by sampling an "off-source" flight data file. This file is a side product of the reduction of the raw flight data. For each event, the ring center position is predicted by the hodoscope. When the ring image is predicted to lie entirely in the photon detector on one side of the instrument, the signals from the opposite side are recorded in a file of "off-source" data. Analysis has shown that there is little correlation in the background with the ring position, making this archive a good representation of the general background in the photon detectors.

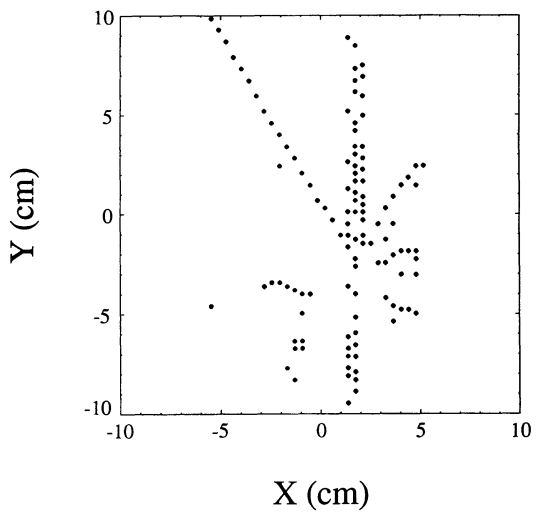

FIG. 9.—The photon detector image of a background event produced by ionizing particles passing directly through the detector volume.

Density Cuts.—While a Čerenkov ring produced by a helium nucleus consists of at most five or six hits around a circle with a maximum diameter of 14.4 cm, a track will trigger virtually every pixel in the photon detector along its length (see Fig. 9). Therefore, by removing events that have dense clusters of hits, such events can be rejected without serious losses for true Čerenkov events. In practice, this is done by investigating a 2 cm diameter circle around every hit that lies within 15 cm of the predicted ring center. If within that circle two additional hits are found, the entire event is removed. This "density cut" removes $\simeq$98% of the background due to tracks but only about 1% of the true Čerenkov rings for helium nuclei.

For nuclei heavier than helium, the density of photons in Čerenkov rings becomes so large that the density cut must be somewhat refined. In this case by including additional information (i.e., the measurement of the nuclear charge Z and the "ring radius" r derived from the distribution of hits) the density of hits in an event can be compared to that expected for a ring. To accomplish this, a "density ratio" is calculated. This is simply the ratio of the average nearest-neighbor separation of hits to the average separation of hits expected for a true Čerenkov ring produced by a nucleus of the measured charge Z and radius r. A cut on this parameter was found to be very useful for all nuclear species with $Z > 2$.

Ring Center Cut.—For high Z nuclei background is also removed by requiring agreement between the independent measurements of the position of the ring center made by the hodoscope and by the fit of a circle to the photon detector data. For Čerenkov rings, the two measurements of the ring center will generally agree to within a few millimeters. If we attempt to fit a circle to a background event, however, the "ring center" found from the fit will not be correlated with the ring center determined by the hodoscopes. By removing such events the background is greatly suppressed without efficiency loss for true events.

Reduced χ^2 and Coincident Background Cuts.—The reduced χ^2 function derived from § 4.4 is used as a measure for the presence of background in the photon detector data. If the reduced χ^2 value is significantly larger than that predicted for a Čerenkov ring, the hits in that event most probably include background. Before cutting out such events, an attempt is made to identify and remove individual coincident background hits. This is accomplished by removing the hits one at a time, in order of their deviation from the average ring radius.[3] If the value of χ^2 cannot be reduced below an acceptable level, the event is rejected. Through Monte Carlo simulations it has been demonstrated that this technique greatly improves the

[3] Only zero, one, or two hits are removed, resulting in the elimination of 90% of the coincident background photons.

efficiency of the χ^2 cut as well as improving the determination of the ring radius.

Figure 10*a* shows a radial histogram of the photon detector hits for helium nuclei around the predicted ring centers, accumulated over the entire flight before the ring analysis cuts have been made. In Figure 10*b* the cuts described above have been performed to remove most of the background from the helium data. Note that a clear edge to the distribution of Čerenkov photons exists at 7.2 cm, corresponding to the maximum possible ring radius. A small residual number of background hits remain, as shown by the tail of photon detector hits extending above the maximum ring radius in Figure 10*b*. Since all this residual background consists of random single-photon hits, the number of such background in any radial bin of this distribution increases with the square of the radius and is negligible at small ring radii. For comparison, the results of a Monte Carlo simulation of the instrument are also plotted in Figure 10*b*. As can be seen, the Monte Carlo simulation accurately reproduces the data, including background.

Each individual helium event contributes several photon hits to the distribution of Fig. 10*b*. The ring radius is fitted to these hits as described in § 4.3.2. The Monte Carlo simulation is then used to determine the distribution of apparent ring radii generated by the residual background. This background contribution to the measured cosmic-ray flux is small, about 8% for the highest energy helium bin. Its quantitative subtraction is discussed below.

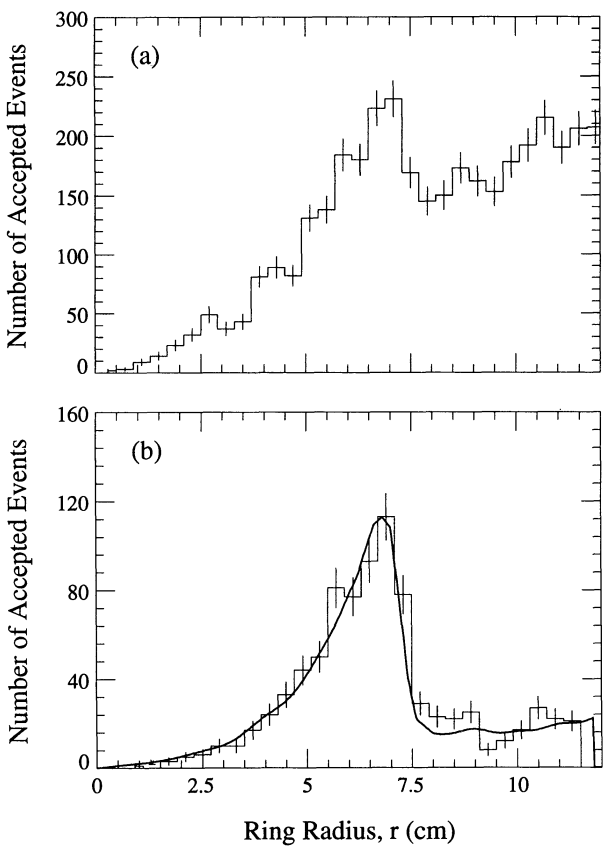

FIG. 10.—Distribution of the detected photoelectrons vs. the radial distance from the predicted ring center, accumulated from the flight helium data (*a*) before data cuts, (*b*) after data cuts. The results of a Monte Carlo simulation are indicated by the solid curve.

4.3.4. *Energy and Flux Determination*

Once a ring radius and then a Lorentz factor has been assigned to each event the data are put into energy bins.[4] The widths of the bins are chosen so that the statistics in each bin are roughly the same. Overlap from neighboring bins—the probability that a particle measured in a high energy bin actually comes from the next lower energy bin—is typically $\sim 12\%$.

The measured flux in each bin is corrected for inefficiencies, remaining background, and the finite energy resolution (overlap corrections) of the instrument, using the matrix equation

$$N_i = \frac{1}{\epsilon_i} \sum_{j=1}^{n} A_{ij}(M_j - \beta_j M_{\text{tot}}) \,. \tag{4.5}$$

Here, N_i is the derived flux for the ith energy bin, M_j is the measured flux for the jth energy bin, A_{ij} is the energy overlap matrix, β_j is the relative background level in the jth energy bin, and ϵ_i is the efficiency for detecting an event in the ith bin, and M_{total} is the total measured flux.

The correction factors A_{ij}, β_j, and ϵ_i are determined from a detailed Monte Carlo simulation of the instrument. Input into this simulation is a power-law spectrum of cosmic-ray events, together with background events. These background events are obtained from the flight data by sampling the photon detector signals *off-source* (i.e., the Čerenkov signals outside the region of expected rings). Other Monte Carlo input parameters that specify energy resolution and detector efficiencies are determined completely from the flight data distributions. The uncertainty in these parameters is used to derive the systematic errors in the measurement. Simulated events are analyzed with the same program that is used for the analysis of the actual flight data.

The energy overlap matrix A_{ij} is constructed directly from the Monte Carlo simulation. The prescription for this is very simple: for each Monte Carlo event (a simulated cosmic ray with or without coincident background), with an energy in bin i leading to a derived energy in bin j, we increment the matrix element α_{ij} and the number n_j. The energy overlap matrix is then given by

$$A_{ij} \equiv \frac{\alpha_{ij}}{n_j} \,. \tag{4.6}$$

The efficiency ϵ_i is accumulated for good Monte Carlo events in bin i which fail to pass the data cuts. The background β_j is accumulated for background Monte Carlo events which pass all of the data cuts and lead to a mistaken assignment of an energy in bin j. The total background level depends on the ratio of cosmic rays with energy above the Čerenkov threshold to the total number of cosmic-ray particles detected. Since this ratio is difficult to predict, an overall normalization factor is applied to β_j so that the background level matches the observed level.

For this simulation, we assume an initial spectral index, δ_0. The value of δ_0 has been found to affect the results only weakly. For example, a difference of 5% between the input value, δ_0, and the correct value, δ, produces only a 0.34% error in determining the true spectral index. To eliminate any error associated with the choice of δ_0, the process of determining the

[4] The kinetic energy E is defined as $E = 0.933(\gamma - 1)$ [GeV nucleon^{-1}].

spectral index is iterated, each time with the latest measured value used as the input parameter.

For redundancy, we have developed two independent computer codes for the Monte Carlo simulation. The deconvolution of the spectrum was performed using these two programs and the results obtained are in excellent agreement.

4.3.5. *Absolute Flux Normalization*

To obtain the absolute flux of cosmic rays entering the instrument, the effective exposure factor of the instrument must be known. This exposure factor includes the live time of the instrument, telemetry efficiency, the geometric acceptance factor, the probability of nuclear interactions in the instrument, as well as the efficiency of the various detectors. The overall effective exposure time of this flight, including all these factors, is ~ 1.4 m^2 sr hr. The detector efficiencies are estimated from the flight data. This ensures that temporal changes in the detector response were taken into account. The factors included in the determination of the flux normalization are listed below.

Live Time.—The live time ratio is easily determined by comparing the raw trigger rate to the transmitted event rate, and by monitoring the status of the detectors throughout the flight. We obtain a total live time of 37,048 s for the present analysis.

Scintillator Trigger Efficiency.—The trigger efficiency of the scintillators was determined to be $\geq 95\%$ for $Z \geq 2$.

Hodoscope Efficiency.—The efficiency of the hodoscope analysis procedure is found to be almost independent of charge. The track reconstruction is aided by the multiple threshold time slice digitization. This helps to identify knock-on electrons, and makes the tracking efficiency high for both light and heavy nuclei since the heavily ionizing region of the track is readily separated from the "halo" of knock-ons. Initially, events with unique tracks are selected, as determined by the adjacent layer correlations discussed in § 4.1. This retains 87% of the helium and 90% of the oxygen events. Then, the goodness of fit of the eight hodoscope signals to a straight line trajectory is also evaluated. We find the rms accuracy of the trajectory fit to be $\sigma \sim 1$ mm. For the further analysis, we reject events with trajectory errors larger than ± 1 mm. This charge-independent geometry cut retains 70% of the data remaining from the uniqueness test, resulting in an overall efficiency of $\sim 63\%$.

Photon Detector.—While drift losses in the photon detector are small, there is a variation in the efficiency for detecting photons for different sense wires, due to variations in the detector and the electronic gain. This efficiency variation is very well mapped out with flight data and is incorporated into the Monte Carlo simulation used to calculate the effective aperture.

Nuclear Interactions in the Instrument.—All particles that undergo charge-changing nuclear interactions with the matter in the instrument are removed by comparing the two charge measurements in the scintillation counters and the eight independent measurements in the hodoscopes and requiring consistency. The photon detector images provide an additional degree of rejection power, especially for the denser rings produced by high Z nuclei (where interactions are the most severe).

The true flux of cosmic rays entering the instrument is then obtained from the flux of accepted events by calculating the nuclear interaction probability in the instrument. Using a Monte Carlo simulation and the properties of the materials used in the construction, the average matter density of the instrument was found to be 13.7 g cm^{-2} (mostly in form of Al and SiO_2). To obtain the total number of interactions, we use the nuclear interaction cross sections from the empirical expression given by Heckman et al. (1978) which is a good approximation for all nuclei in the projectile and the target except hydrogen. For this special case, the cross sections are obtained from the Review of Particle Properties (1992).

Nuclear Interactions in the Atmosphere.—The fluxes of nuclei measured at the instrument are corrected to the top of the atmosphere by a numerical solution of the transport equation. For the transport of nuclei through the atmosphere, total collision cross sections are taken from Heckman et al. (1978), and partial production cross sections on air are scaled from the proton-nucleus values of Silberberg & Tsao (1973) by the factorization method of Heckman & Greiner (1972). The instrument deadtime variations and flight altitude history are taken into account by solving the transport equations for every 15 minute interval throughout the flight. By this method helium was determined to have suffered atmospheric losses of $\sim 12\%$ and the losses for carbon are $\sim 20\%$. The accuracy of this correction is determined by cross section uncertainties ($\sim 10\%$), translating to an uncertainty in the absolute fluxes of about 1%–2%.

4.3.6. *The Differential Energy Spectrum*

After unfolding the energy spectrum and correcting for the effective aperture of the instrument, the flux N_i in the ith energy interval is related to the differential cosmic-ray energy spectrum by

$$N_i = \int_{E_i}^{E_{i+1}} \frac{dN}{dE}\, dE\,, \tag{4.7}$$

where (E_i, E_{i+1}) is the energy interval for N_i, and dN/dE is the differential flux.

Assuming that within each bin the differential energy spectrum is given by the power law $\sim E^{-\delta}$, the median energy is given by

$$E_{m,i} = [(E_i^{1-\delta} + E_{i+1}^{1-\delta})/2]^{1/1-\delta}\,, \tag{4.8}$$

and the differential flux at $E_{m,i}$ is

$$\left.\frac{dN}{dE}\right|_{E_{m,i}} = N_i \left[\frac{(\delta - 1)}{E_i^{(1-\delta)} - E_{i+1}^{(1-\delta)}}\right] E_{m,i}^{-\delta}\,. \tag{4.9}$$

The resulting values depend upon the input spectral index δ used. This dependence, however, is weak. To reduce any possible errors an iterative process is used in estimating δ.

5. RESULTS AND DISCUSSION

The differential flux of helium, carbon, and oxygen, extrapolated to the top of the atmosphere, is presented in Table 1. The errors given are statistical. Due to the residual uncertainties in the instrument acceptance aperture the systematic error in the absolute normalization of these data is about 15%. The systematic uncertainty in the flux *ratios* of different elements is much smaller, about 2%.

In addition to the energy spectrum obtained from the Čerenkov analysis above ~ 40 GeV nucleon^{-1}, we also show in the table a differential flux measurement at lower energy utilizing the geomagnetic cutoff rigidity. For this measurement, a subset of the data was selected for which the balloon was essentially stationary at a fixed geomagnetic cutoff rigidity. For this period (approximately 20 minutes), the vertical geomag-

TABLE 1

FLUXES OF NUCLEI MEASURED BY THE RICH EXPERIMENT

Element	Energy nucleon^{-1} (GeV nucleon^{-1})	Number of Events[a]	Differential Flux (m^2 sr s GeV nucleon)$^{-1}$	
Helium	4.2	9460	9.13	± 0.01
	48.0	96	2.36×10^{-2}	$\pm 2.8 \times 10^{-3}$
	59.7	175	1.32×10^{-2}	$\pm 1.4 \times 10^{-3}$
	79.0	135	6.02×10^{-3}	$\pm 6.4 \times 10^{-4}$
	125.2	128	1.80×10^{-3}	$\pm 2.1 \times 10^{-4}$
	314.4	124	1.68×10^{-4}	$\pm 2.6 \times 10^{-5}$
Carbon	4.2	268	2.37×10^{-1}	$\pm 1.4 \times 10^{-2}$
	48.1	25	9.4×10^{-4}	$^{+2.6}_{-2.1} \times 10^{-4}$
	71.4	12	2.6×10^{-4}	$^{+1.1}_{-0.8} \times 10^{-4}$
	138.9	18	5.5×10^{-5}	$^{+1.9}_{-1.5} \times 10^{-5}$
Oxygen	4.2	214	2.02×10^{-1}	$\pm 1.4 \times 10^{-2}$
	48.1	15	5.9×10^{-4}	$^{+2.3}_{-1.8} \times 10^{-4}$
	71.4	15	3.3×10^{-4}	$^{+1.2}_{-0.9} \times 10^{-4}$
	138.9	15	5.2×10^{-5}	$^{+2.0}_{-1.5} \times 10^{-5}$

NOTE.—The fluxes at 4.2 GeV nucleon^{-1} are derived by a geomagnetic method described in the text.

[a] Before background subtraction.

netic cutoff was 5.03 GV, corresponding to a kinetic energy cutoff of 1.75 GeV nucleon^{-1} for nuclei with $A = 2Z$. To represent this integral measurement in differential form, knowledge of the spectral slope is required. We use the spectral slope measured at high energy after applying an appropriate correction for solar modulation.

The energy spectrum of He nuclei as determined in this measurement is shown in Figure 11 where the fluxes have been multiplied by $E^{2.75}$. For comparison, we include data from previous measurements by other workers. Our results indicate a higher helium flux above ~ 100 GeV nucleon^{-1} than the high-energy data points of Ryan et al. (1972). As Figure 11 shows, it appears that our data relieve somewhat the discrepancy in the spectrum between previous measurements made above and below 1 TeV nucleon^{-1}. A power-law fit to our data over the range 40 GeV nucleon^{-1} to 300 GeV nucleon^{-1} yields a spectral index $\delta = 2.64 \pm 0.09$.

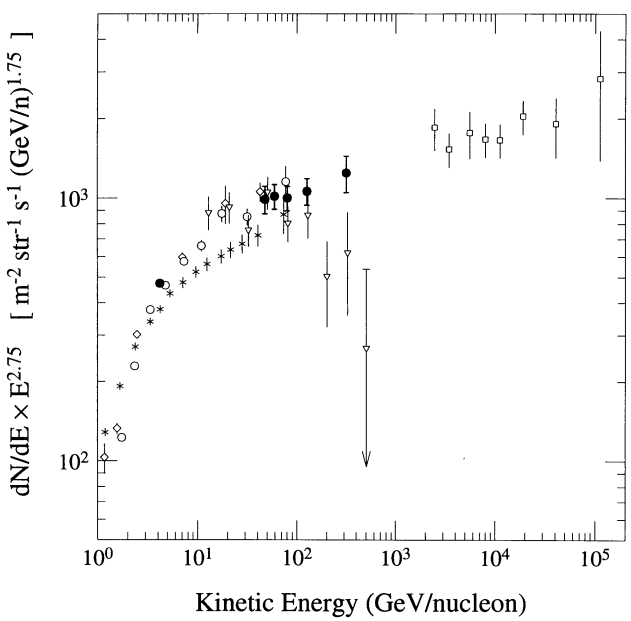

FIG. 11.—The energy spectrum of cosmic-ray helium (*filled circles*: present results; *squares*: Asakimori et al 1993; *triangles*: Ryan et al. 1972; *open circles*: Smith et al. 1973; *diamonds*: Von Rosenvinge et al. 1969; ×'s: Seo et al. 1991).

In Figure 12, we show the results of the present measurement of helium together with our data on carbon and oxygen. The data are compared with a compilation of data from measurements in space (Engelmann et al. 1990; Müller et al. 1991) and on balloons (Ryan et al. 1972; Smith et al. 1973; Asakimori et al. 1993). We also include the existing hydrogen data from balloon experiments, although our present measurement did not include this species. Note that the differential spectra are multiplied with $E^{2.75}$. While our flux measurements of the heavier cosmic-ray nuclei are limited by counting statistics, we notice good agreement with the earlier data for carbon and oxygen, within the published systematic uncertainties in the flux normalizations of these measurements. This gives us confidence that our spectrum for helium represents the correct absolute flux, within a 15% normalization uncertainty.

The measurement of the proportion of nuclei predominantly produced by spallation in the interstellar medium has long been established as a key monitor for cosmic-ray propagation through the galaxy. In this work we have obtained measurements of the ratios of Li/C, Be/C, and B/C at the top of the atmosphere which are tracers of this type, as they are essentially absent in the source. Figure 13 shows our data, together with some previous determinations, as a function of particle energy. These new results are consistent with previous measurements. The curves shown in Figure 13 represent the parameterization of the propagation path lengths used by Swordy et al. (1990). Although the statistics in our new data are limited we believe that the future use of RICH detectors for the measurement of the secondary/primary ratio will be highly desirable, because of the complete independence of charge and energy measurements with such devices. Given sufficient exposure factors, this should permit accurate measurements of neighboring charges (such as B/C) even if the abundance ratios are as large as 50 or more.

In our previous work (Swordy et al. 1993), we had used a simple leaky box model of galactic propagation to interpret the spectra of heavy nuclei ($Z \geq 5$) as measured on *HEAO 3* (Engelmann et al. 1990) and on Spacelab 2 (Müller et al. 1991).

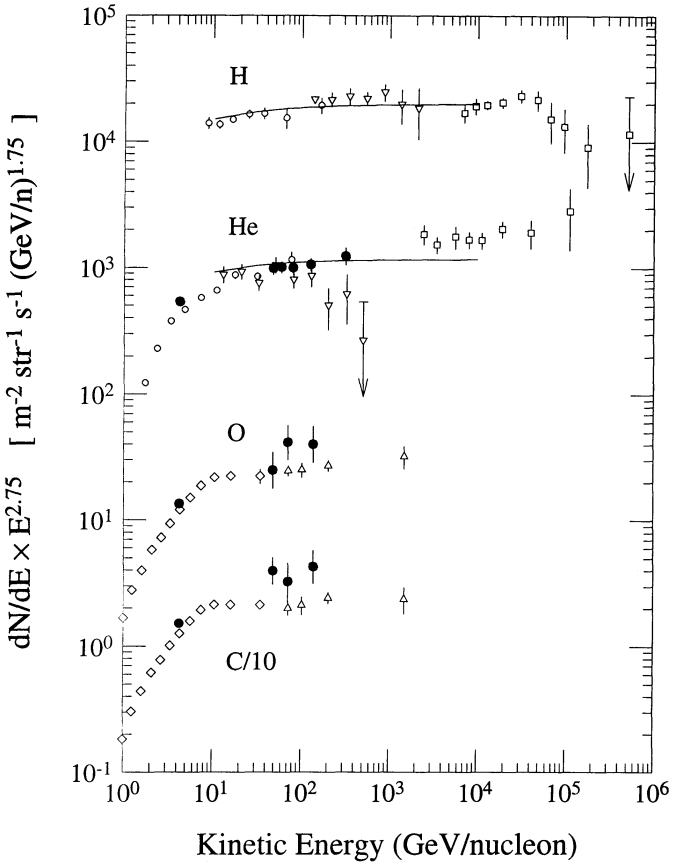

FIG. 12.—Compilation of differential spectra (multiplied by $E^{2.75}$) for H, He, C, and O. Note that the scale for carbon is reduced by a factor of 10 in order to avoid overlap between C and O (*filled circles*: our results; *squares*: Asakimori et al. 1991; *diamonds*: Ryan et al. 1972; *open circles*: Smith et al. 1973; *triangles*: Müller et al. 1991; *diamonds*: Engelmann et al. 1990). Solid lines refer to a leaky box propagation model (see text).

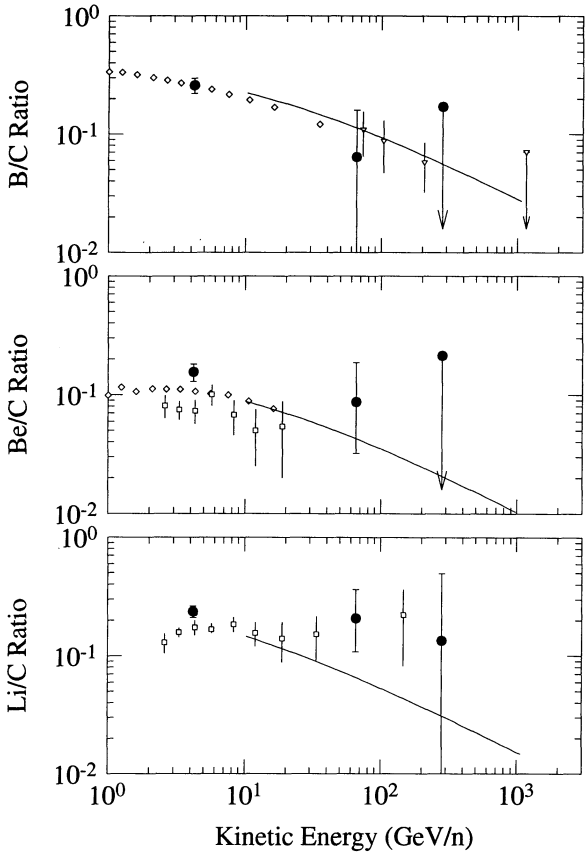

FIG. 13.—Abundances of the secondary nuclei Li, Be, and B, relative to carbon. (*filled circles*: present results; *diamonds*: Engelmann et al. 1990; *squares*: Smith et al. 1973; *triangles*: Swordy et al. 1990a, b).

We found good agreement with the predictions of such a model if we assumed that all primary nuclear cosmic-ray species are accelerated at the source with the same power law $\propto E^{-2.2}$, and that the interstellar propagation path length decreases with particle rigidity R as

$$\lambda(R) = 6.9\left(\frac{R}{20\ \mathrm{GV}}\right)^{-0.6}\ \mathrm{g\ cm^{-2}}\ .$$

The curves shown on Figures 12 and 13 are fits which use this propagation path length dependence and constrain the source spectra of all elemental species to the same power law $\propto E^{-2.15}$. As Figure 12 shows, this model clearly fits both the proton measurements and the new data on helium in the energy region ~50–500 GeV nucleon^{-1}. The oxygen and carbon fluxes reported here, while consistent with this model, do not seriously constrain the spectral slope.

We use this model to propagate the absolute cosmic-ray intensities measured near Earth to the acceleration site and to determine the relative elemental abundances at the source. In particular, we derive from the fluxes reported here the cosmic-ray source abundance of helium relative to oxygen. This provides a value which is free from the systematic uncertainties present when comparing fluxes from different experiments. We obtain a relative abundance of helium to oxygen in the cosmic-ray source of 25 ± 6 at ~100 GeV nucleon^{-1}. The uncertainty is dominated by the statistical error in the oxygen flux.

It is now well known that the elemental abundances at the cosmic-ray source relative to the local galactic values appear to decrease with increasing first ionization potential (FIP) of the elements. For heavy elements ($Z > 4$) this feature has been observed up to energies of ~100 GeV nucleon^{-1} and beyond (Müller et al. 1991). Figure 14 shows these earlier results and includes our new data on the relative abundance of helium ~100 GeV nucleon^{-1}. We note that the mean propagation path length of particles at this energy is just ~2 g cm^{-2}. Consequently, the effects of propagation on the relative abundances of primary cosmic rays can be more reliably determined at ~100 GeV nucleon^{-1} than at lower energies.

6. CONCLUSION

We have presented a new measurement of the spectrum of cosmic-ray helium nuclei covering an energy region where previous data are scarce and controversial. Our detector has simultaneously provided results on heavier nuclei up to oxygen which are in good agreement with previous measurements in space that use entirely different techniques. This fact lends credence to our new experimental approach, using ring imaging Čerenkov counters. This technique is characterized by high immunity against background and high accuracy in the energy determination. While our results are still limited by counting statistics, future balloon flights of this instrument should reduce this uncertainty.

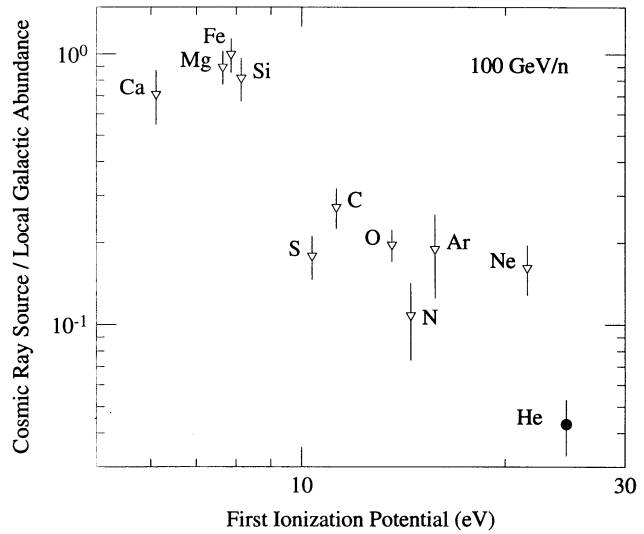

FIG. 14.—Cosmic-ray source abundances relative to the local galactic elemental abundances at 100 GeV nucleon^{-1} vs. the first ionization potential of the elements. The solid point for helium is obtained in the present investigation, while the open triangles are from Müller et al. (1991).

However, within the error limits of the presently available data, we find that the simple leaky box model is a good fit to the proton and helium data over the energy range $\sim$50–500 GeV nucleon^{-1}. The single source energy spectrum which best fits these data has the form $\propto E^{-2.15}$. This is very close to the source spectra for heavy nuclei in this energy range, derived previously by Müller et al. (1991) and Swordy et al. (1993). We may conclude that the elemental composition of the cosmic-ray source shows no sign of energy dependence in this region. The spectral index at the source is very close to that expected from first-order Fermi acceleration involving strong shocks ($\propto E^{-2}$), supporting supernova shock acceleration as the most probable source mechanism.

The elemental composition of the cosmic-ray source is clearly different from that of local galactic material. This is most clearly seen in the depletion of elements with high FIP. Our data show (Fig. 14) that helium at the cosmic-ray source is more strongly suppressed than the other elements. This depletion has been noticed at lower energies as well (see, e.g., Webber et al. 1990). It has frequently been argued that the correlation of cosmic-ray abundances with the FIP could be parametrized by a step function, such that elements with FIP < 10 eV show very little depletion elements with FIP > 10 eV are all depleted by about the same factor. This model cannot be supported by our results on helium. We find that the abundance ratio of helium to oxygen in the source is about 25, as compared to the local galactic ratio of 115 (Meyer 1985). It is interesting to note that a very similar depletion of helium has also been observed for solar energetic particles. Here, a helium-to-oxygen abundance ratio of about 55, intermediate between the cosmic ray and the local galactic values, has been reported (Reames et al. 1991). The depletion of elements with high ionization potential for solar particles may be ascribed to a fractionation process during the transport of material containing neutral atoms from the photosphere to the solar corona (von Steiger & Geiss 1989). Perhaps a similar process acting at an even longer timescale than on the Sun has produced the seed population of suprathermal charged particles which are then accelerated to become high-energy cosmic rays.

We thank the engineering staff of the Laboratory for Astrophysics and Space Research of the University of Chicago for making this technically challenging experiment possible. In particular, D. E. Bonasera, E. Drag, W. C. Johnson, and D. Plitt made invaluable contributions to this effort. We also greatly appreciate the excellent services of the team of the National Scientific Balloon Facility led by D. Gage and D. Ball. This work was supported in part by NASA grants NSG 7464, NSG W-1995, NASA GSRP grants NGT 50272 and NGT 50463; additional support came from the Department of Physics and the Block Fund of the University of Chicago.

REFERENCES

Anderson, D. F. 1981, IEEE Trans. Nucl. Sci. Ns-28, 842
———. 1982, Physics Letters 118B, 230
Apsimon, R. J., et al. 1985a, IEEE Trans. Nucl. Sci. Ns-32, 674
Apsimon, R. J., et al. 1985b, Meth. A241, 339
Asakimori, K., et al. 1993, Proc. 23rd Int. Cosmic Ray Conf. (Calgary), 2, 21
Buckley, J., Dwyer, J., Müller, D., Swordy, S., & Tang, K. K. 1992, Nucl. Instr. and Meth. A323, 380
———. 1993, Proc. 23rd Int. Cosmic Ray Conf. (Calgary), 1, 599
Dwyer, J., Buckley, J., Müller, D., Swordy, S., & Tang, K. K. 1993, Proc. 23rd Int. Cosmic Ray Conf. (Calgary), 1, 587
Ellison, D. C. 1993, Proc. 23rd Int. Cosmic Ray Conf., Calgary, 2, 219
Engelmann, J. J., et al. 1990, A&A, 233, 96
Heckman, H. H., & Greiner, D. E. 1972, Phys. Rev. Letters, 28, 926
Heckman, H. H., Greiner, D. E., Lindstrom, P. J., & Shwe, H. 1978, Phys. Rev. C 17, 1735
Holroyd, R. A., Preses, J. M., Woody, C. L., & Johnson, R. A. 1987, Nucl. Instr. and Meth. A261, 440
L'Heureux, J., Grunsfeld, J. M., Meyer, P., Müller, D., & Swordy, S. P. 1990, Nucl. Instr. and Meth. A295, 246
Meyer, J. P. 1985, ApJS, 57, 173
Müller, D., Swordy, S. P., Meyer, P., L'Heureux, J., & Grunsfeld, J. M. 1991, ApJ, 374, 356
Review of Particle Properties, Phys. Rev., D45, Part 2 (1992)
Reames, D. V., Richardson, I. G., & Barbier, L. M. 1991, ApJ, 382, L43
Ryan, M. J., Ormes, J. F., & Balasubrahmanyan, V. K. 1972, Phys. Rev. Letters, 28, 15, 985
Seo, E. S., Ormes, J. F., Streitmatter, R. E., Stochaj, S. J., Jones, W. V., Stephes, S. A., & Bowen, T. 1991, ApJ, 378, 763
Silberberg, R., & Tsao, C. H. 1973, ApJS, 25, 315
Smith, L. H., Buffington, A., Smoot, G. F., Alvarez, W., & Wahlig, M. A. 1973, ApJ, 180, 987
Swordy, S. P., Müller, D., Meyer, P., L'Heureux, J., & Grunsfeld, J. 1990, ApJ, 349, 625
Swordy, S. P., L'Heureux, J., Meyer, P., & Müller, D. 1993, ApJ, 403, 658
Von Rosenvinge, T. T., Webber, W. R., & Ormes, J. F. 1969, Astrophys. Space Sci., 5, 342
von Steiger, K. G., & Geiss, J. 1989, A&A, 225, 222
Webber, W. R., Soutoul, A., Ferrando, P., & Gupta, M. 1990, ApJ, 348, 611
Wilkinson, P. G. 1960, J. Opt. Soc. Am., 50, 1002